Methodology for a mechano-electrochemical evaluation of the coupling at the crack tip. Application of halide-induced Stress Corrosion Cracking of Zircaloy-4

E. Durif, Marion Fregonese, Julien Réthoré, A. Combescure, C. Alemany-Dumont

Methodology for a mechano-electrochemical evaluation of the coupling at the crack tip. Application of halide-induced Stress Corrosion Cracking of Zircaloy-4

Emilien Durif [a], Marion Fregonese [b,*], Julien Réthoré [a], Alain Combescure [a], Catherine Alemany-Dumont [b]

[a] INSA-Lyon, LaMCoS UMR 5259, 69621 Villeurbanne cedex, France
[b] INSA-Lyon, MATEIS UMR 5510, 69621 Villeurbanne cedex, France

In order to evaluate the relative contribution of both mechanical and electrochemical processes at the crack tip during Stress Corrosion Cracking propagation, an original combination of controlled pre-cracking followed by thermal pre-oxidation of SCC specimens was developed. It allowed localizing dissolution at the crack tip for Zircaloy-4 tested in halide solutions under potentiostatic polarization. Digital Image Correlation and electrochemical methods were then carried out to study correlations between the stress intensity factor, the crack length and the measurements of dissolution current.

1. Introduction

Stress Corrosion Cracking (SCC) in metallic alloys is still a serious problem in many industrial domains such as the oil and gas, chemistry and nuclear industries. Any attempts at modeling the elementary processes of SCC induced degradation of structural materials, in order to estimate component lifespan, are indeed worthy of interest.

In spite of several attempts, it remains impossible to establish a universal theory on all metal/medium SCC systems [1,2]. Most studies related to SCC consider the crack rate propagation ($\frac{da}{dt}$) the main interest. Due to the synergetic nature of SCC, the crack propagation rate appears to depend on both mechanical (σ^*) and electrochemical (χ^*) parameters [2–5]:

$$\frac{da}{dt} = f(\sigma^*, \chi^*) \tag{1}$$

Relative and mutual influences of σ^* and χ^* can be approached from experimental procedures allowing the estimation of $\frac{da}{dt}$ in real time and the identification of relevant σ^* and χ^* parameters.

χ^* parameter estimation mainly consists of evaluating the dissolution current density j at the crack tip while $\frac{da}{dt}$ can be related to j by local Faraday's law [2]:

$$\frac{da}{dt} = \frac{M \cdot j}{z \cdot F \cdot \rho} \tag{2}$$

(M: molar mass of the dissolved species, z: number of electrons exchanged during dissolution, F: Faraday's constant, ρ: density of the corroding metal.)

From an electrochemical point of view, three possibilities of evaluating j are offered:

(i) electrochemical noise measurements at the Open Circuit Potential (OCP), with the evaluation of the exchanged current density between the working electrode and an inert electrode; this method was successfully applied by several authors [6–11] to detect SCC initiation; yet, current fluctuations at the crack tip can turn out to be undetectable when the crack has propagated;
(ii) galvanostatic polarization with difficulty in promoting crack tip dissolution toward pitting and ensuring the repassivation of crack the mouth during propagation;
(iii) current density measurement under potentiostatic polarization over the depassivation potential at the crack tip.

The latter can be considered with a SCC system such as a zirconium alloy in halide solution, leading to intergranular and transgranular propagation of SCC cracks when polarized over the pitting potential [12–14].

On the other hand, rupture mechanics at the crack tip shows evidence of the predominance of the mode I stress intensity factor (SIF) K_I among σ^* parameters as a defining criterion of propagation. Actually, K_I is commonly used in SCC models [4,15] as observed fractures present fragile features, even if plastic deformation must remain sufficiently confined to the crack tip to keep this approach

* Corresponding author.
E-mail address: marion.fregonese@insa-lyon.fr (M. Fregonese).

valid [16]. Moreover, chemical damage at the crack tip can be governed by the crack mouth opening or the emergence of slip bands. Variations of K_I ($\dot{K}_I$) can therefore also be placed under consideration.

In order to experimentally reach the instantaneous values of the crack length a and K_I, the Digital Image Correlation (DIC) technique was successfully used for evaluating SCC or fatigue–corrosion processes [17–20]. DIC is a full displacement field measurement method based on the optical flow equation. It assumes that the gray level variation at the sample surface is only due to the displacement field u. From the knowledge of two gray level functions, f for the reference state and g for the deformed state, the displacement field u is searched for. It is stated that this displacement field minimizes the quadratic gap Φ between the reference image f and the deformed image corrected by the displacement $g(z+u)$:

$$\Phi = \Sigma[f(z) - g(z+u)]^2 \tag{3}$$

where $z = x + iy$ denotes the position of a pixel in the local frame of the crack tip in the reference image. Assuming a small solution increment du between two iterations, Eq. (3) can be linearized to obtain a quadratic form in du:

$$\begin{aligned}\Phi &= \Sigma[f(z) - g(z+u+du)]^2 \\ &= \Sigma[f(z) - g(z+u)]^2 + 2\Sigma[du \cdot g'(z+u)] \cdot [f(z) - g(z+u)] \\ &\quad + \Sigma[du \cdot g'(z+u)]^2\end{aligned} \tag{4}$$

In this equation g' is the spatial derivative of g. The minimization of this equation with respect to du leads to a linear system. This process is run until convergence is reached on the solution increment. In the general case, finite element functions can be used to describe the displacement field in Eq. (4). In this case, once the displacement has been calculated, its derivatives can be computed to evaluate strains or Green–Lagrange strains as shown later. In the case of crack propagation, a specific decomposition of the displacement is used for solving this system (Eq. (4)). The Williams' series [21] that described the displacement field around the tip of a crack in an elastic solid are used latter on to decompose the displacement field. Using these series, the unknown displacements are directly related to known factors such as stress intensity factors and the distance to the crack tip. Indeed, the Williams' series are written as:

$$\Omega_n = \frac{r^{n/2}}{2\mu\cdot\sqrt{2\pi}}\left[\kappa\exp\left(i\frac{n}{2}\theta\right) - \frac{n}{2}\exp\left\{i\left(2-\frac{n}{2}\right)\theta\right\} + \left((-1)^n + \frac{n}{2}\right)\exp\left\{-i\frac{n}{2}\theta\right\}\right] \tag{5}$$

for mode I, and:

$$Y_n = \frac{ir^{n/2}}{2\mu\cdot\sqrt{2\pi}}\left[\kappa\exp\left(i\frac{n}{2}\theta\right) + \frac{n}{2}\exp\left\{i\left(2-\frac{n}{2}\right)\theta\right\} - \left((-1)^n + \frac{n}{2}\right)\exp\left\{-i\frac{n}{2}\theta\right\}\right] \tag{6}$$

for mode II. The searched displacement thus reads

$$u = \Sigma_n(\Omega_n a_n + Y_n b_n) \tag{7}$$

In these expressions $z = r \times \exp(i\theta)$, where r and θ denote the in-plane coordinates linked to the usual crack tip frame for a given position of the crack tip, μ is Lamé's shear modulus, and κ a dimensionless elastic (or Kolossov) coefficient related to Poisson's ratio v according to $(3 - v)/(1 + v)$ for plane stress conditions or $3 - 4v$ for plane strain conditions. For mode I and mode II, the terms corresponding to $n = 1$ are the stress intensity factors K_I ($a_1 = K_I$) and K_{II} ($b_1 = K_{II}$). Furthermore, following Roux and Hild [22], the first super-singular term a_{-1} ($n = -1$) is used to evaluate the distance d to the equivalent elastic crack tip using the following formula:

$$d = \frac{-2a_{-1}}{a_1} \tag{8}$$

From the resolution of Eq. (3) using the decomposition of u given in Eq. (7), the crack tip position is updated and the process is repeated until convergence is reached on the crack tip position. Then, the crack length and stress intensity factors value are stored and the next deformed image is treated. For a healthy estimation of the DIC degree of freedom, it is required that the local variation of the gray level is produced only by the displacement field. This means that uncontrolled modification of the surface's aspect must be avoided.

As mentioned above, DIC was recently applied in fatigue–corrosion to monitor crack growth by measuring opening defect displacements [20]. The present authors also successfully used this technique to perform the fatigue pre-crack of SCC specimens at controlled SIF, allowing the control of plasticity at the pre-crack tip prior to the SCC test [23]. The developed methodology, based on a load-shedding technique, is applied in the present study for specimen preparation.

In this context, the main objectives of the present study are (i) the localization of dissolution at the crack tip during SCC propagation and (ii) the real-time evaluation of current density j, the crack length a and mode I SIF K_I and their correlations.

2. Local electrochemistry modeling at crack tip

As mentioned above, the quantitative evaluation of dissolution effects on the crack propagation rate is usually obtained through the estimation of the local current density j at the crack tip. As electrochemical measurements only give the value of the global dissolution current I under potentiostatic polarization, it is therefore necessary to consider that the electrochemically active area S_χ is constant during crack displacement and is located at the crack tip [2] (Fig. 1) in order to get a quantitative estimation of the loss of metal by local dissolution.

In the case of zirconium dissolution, the main anodic contribution is the result of Eq. (9).

$$\mathrm{Zr} \rightarrow \mathrm{Zr}^{4+} + 4\mathrm{e}^- \tag{9}$$

The consecutive molar number of dissolved zirconium atoms is therefore given by Eq. (10):

$$n_{\mathrm{Zr}} = \frac{q}{4F} \tag{10}$$

F being Farraday's constant and q the exchanged charge.

Consequently, the elementary volume created by Zr dissolution, dV_χ, can be calculated through Eq. (11):

$$dV_\chi = \frac{dq \cdot M}{4\rho F} \tag{11}$$

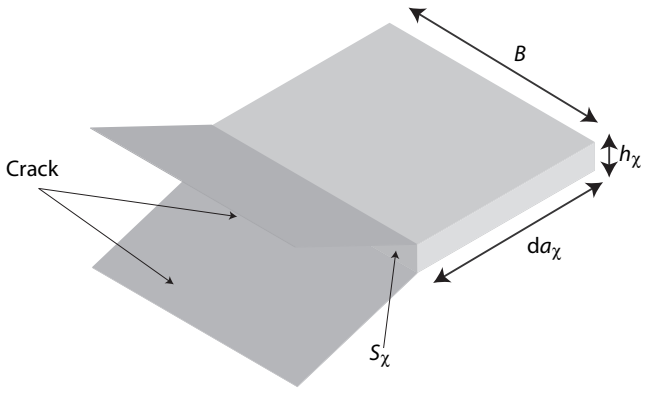

Fig. 1. Modeled geometry of the crack tip.

with ρ: Zr density (=6.52 g cm^{-3}) and M: Zr molar mass (=91.41 g mol^{-1}).

On the other hand, literature devoted to SCC modeling involving dissolution processes [2,4,15,24] consider that crack propagation is the result of the creation of a dissolved volume at the crack tip. According to Fig. 1, V_χ can therefore also be calculated by:

$$dV_\chi = da_\chi \cdot S_\chi = da_\chi \cdot B \cdot h_\chi \tag{12}$$

Combining Eqs. (11) and (12), h_χ is obtained by:

$$h_\chi = \frac{M \cdot dq}{4\rho F \cdot B \cdot da_\chi} = \frac{M \cdot I dt}{4\rho F \cdot B \cdot da_\chi} \tag{13}$$

If crack propagation is governed by dissolution, it can be considered that $da_\chi = da$. Moreover, if the initial hypothesis of the constant dissolution area localized at the crack tip is verified, it is therefore possible to calculate a constant value of h_χ during crack propagation, by measuring I, integrating $I\,dt$ by the trapeze method and evaluating Δa in real-time by Digital Image Correlation. The value of h_χ and its evolution will be the indicator of the methodology relevance.

In this context, experimental conditions must allow to maintain a passive state for notched and pre-cracked areas, as well as ensuring the repassivation of the crack mouth of the SCC propagating crack.

As previously mentioned, smooth Zircaloy-4 specimens are known to be prone to SCC in halide aqueous solutions if polarized above the pitting potential [13,14]. Yet, on pre-cracked specimens, pits would then initiate randomly on all the exposed areas and not only at the crack tip. In order to reach the main objective of this work, it is proposed a thermal pre-oxidation of the pre-cracked tensile specimens be applied, then polarizing them near the pitting potential of the non-oxidized metal. The effect of thermal oxidation on pitting potentials is studied in Section 4.1. In these conditions, it is expected that the measured dissolution current I is the result of local emerging slip bands dissolution at crack tip (Fig. 2).

The experimental procedure was defined to study the conditions of obtaining the above SCC process induced by dissolution.

3. Experimental procedure

3.1. Material and specimen preparation for DIC and SCC tests

Transverse tensile test specimens were machined out in a 2.92 mm thick sheet of recrystallized Zircaloy-4 provided by CEZUS, whose composition and mechanical properties are given in Tables 1 and 2 respectively.

Specimens were pre-cracked following the procedure based on the load-shedding technique detailed in [23]. Fatigue tests were first performed on Zircaloy-4 tensile test samples which were notched to localize crack initiation. The sample was designed with a $S = 2.92 \times 8$ mm^2 section (Fig. 3). The notch was 0.5 mm in length. During the fatigue test a digital camera was used to take pictures of the sample surface. A speckle was applied on it using a white then a black paint spray to generate random gray level distribution. Then the methodology proposed in [23] was used to evaluate the evolution of crack propagation and to stop the fatigue pre-cracking once a given crack length was obtained. After pre-cracking, the speckle was removed and the specimens were thermally oxidized in air at 470 °C for 40 h. A new speckle was applied after oxidation and before the SCC test, using a white then a black paint spray.

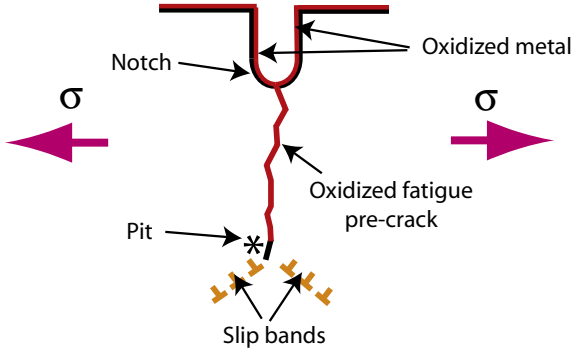

Fig. 2. Localization of anodic dissolution at crack tip by thermal oxidation.

3.2. Experimental setup

During SCC testing, the gauge length of the pre-cracked and thermally pre-oxidized specimen was immersed in a 350 mL cell containing the aggressive solution. Two aqueous 0.5 M KBr and 0.5 M NaCl solutions were tested. They were prepared from high purity NaCl and KBr grades and were de-aerated by continuous nitrogen bubbling.

In order the characterize pitting, potentiostatic polarization was applied by an EG&G 273A potentiostat. The counter electrode was a graphite bar and a Saturated Calomel Electrode (SCE) was used as the reference electrode.

Complementary Electrochemical Impedance Spectroscopy (EIS) experiments were carried out with a Gamry Ref 600 potentiostat. The tested amplitude and frequency domains were ±10 mV/OCP and [10^{-2}; 10^5 Hz] respectively.

The cell was designed in order to ensure both electrochemical polarization conditions (3 electrodes setup + de-aeration) and DIC measurements. It was therefore equipped with a Plexiglas® flat window and two immersed optical fibers for in-situ lightning (Fig. 4). For DIC measurements, a telecentric objective (Blue Fox camera with a 1200 × 1600 pixel resolution CCD sensor) was used to avoid artificial dilatation due to out-of-plane displacement that can be induced by necking phenomena.

The error on the value of K_I induced by the presence of both the Plexiglas window and the liquid between the objective and the specimen surface, was estimated to be lower than 2%.

Mechanical solicitation during SCC experiments consisted of constant force testing performed at 3200 N on a MTS tensile machine of 10 kN capacity or Slow Strain Rate Tests (SSRT) conducted at 1.4×10^{-6} s^{-1}, until final rupture of the specimens. After failure, fracture surfaces were observed by Scanning Electron Microscopy (SEM).

4. Results and discussion

4.1. Localization of dissolution at the crack tip

The first objective of this study was to ensure and measure local dissolution at the crack tip. For this purpose, it was chosen to oxidize the pre-cracked specimens at 470 °C for 40 h in air and to further polarize the pre-oxidized specimen above the pitting potential of the non-oxidized metal, under tensile stress.

This temperature being lower than the recrystallization temperature of Zircaloy-4, it was therefore considered that the mechanical properties were not affected by the thermal treatment. In these conditions, the oxide thickness should reach some tenths of microns [25]. No previous study refers to the evolution of the electrochemical properties of metal/solution interface with the oxide thickness in aqueous KBr or NaCl solutions. Yet, Sidky [26] proved that an oxide thickness higher than 0.5 μm ensured electrical insulation of Zircaloy-4 in iodine solutions.

Table 1
Composition (Zr: balance).

Cr (%)	Fe (%)	O (%)	Sn (%)	Al (ppm)	C (ppm)	Hf (ppm)	N (ppm)	Ni (ppm)	Si (ppm)
0.11	0.21	0.13	1.32	20	139	57	28	22	102

Table 2
Mechanical properties of the studied Zircaloy-4 sheet, obtained by global measurements and DIC (σ_Y: 0.2% yield strength, σ_M: plastic instability stress, A: ductility at failure, E: Young's modulus, ν: Poisson's coefficient).

σ_Y (±10 MPa)	σ_M (±10 MPa)	A (±1%)	E (±1 GPa)	ν (±0.01)
360	411	23	93	0.37

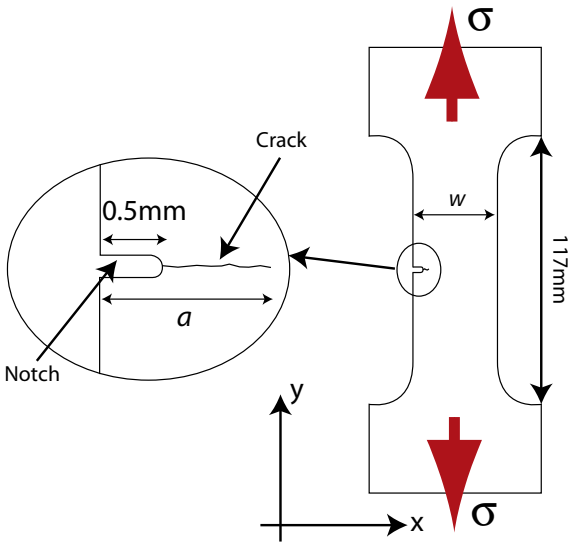

Fig. 3. Specimen, pre-notch and pre-crack geometry.

The effect of pre-oxidation was studied by Electrochemical Impedance Spectroscopy (EIS) experiments performed in a 0.5 M NaCl solution. The electrochemical behavior of the interface can be modeled by a Randle's circuit: the electrolyte resistance R_e in series with the polarization resistance R_p and total (space charge + double layer) capacity C associated in parallel [27,28]. Electrochemical impedance is therefore given by:

$$Z(f) = R_e + \frac{R_p}{1 + i \cdot 2\pi \cdot f \cdot R_p \cdot C} = R_e + \frac{R_p(1 - i \cdot 2\pi \cdot f \cdot R_p \cdot C)}{1 + (2\pi \cdot f \cdot R_p \cdot C)^2} \quad (14)$$

Fig. 5a and b shows the Nyquist diagrams drawn for non-oxidized and oxidized specimens respectively. They both exhibit a capacitive behavior of the film/oxide. It can be noted that the R_p value for non-oxidized Zircaloy-4 is in keeping with previous study results obtained for Zircaloy-2 in an aqueous NaCl solution [29]. For the pre-oxidized specimen, R_p is about $10^8\ \Omega\,cm^2$, which is 100 times higher than before and which confirms the highly protective character of the thermal oxide. Experimental results also confirmed the very low value of R_e, which validates the chosen modeling of interface electrochemical behavior.

The capacity C can be estimated by considering an asymptotic behavior for high frequencies. Imaginary part of impedance (Im(Z)) can thus be approached by:

$$\mathrm{Im}(Z(f \gg 1)) = -\frac{1}{C \cdot 2\pi \cdot f} \quad (15)$$

As $\mathrm{Im}(Z) \times 2\pi \cdot f$ tends to stabilize for $f > 10^5$ Hz, C can be estimated at 0.19 $\mu F\,cm^{-2}$.

R_p and C values were obtained from parameter adjustment thanks to Eq. (14) with an error value ($\chi 2$) equal to 3.6×10^{-4}.

The oxide thickness t_{ox} is determined thanks to the capacitance formula (16) [30].

$$t_{ox} = \frac{\epsilon_{Zr} \cdot \epsilon_0 \cdot A_\chi}{C} \cong 0.11\ \mu m \quad (16)$$

It is reversely proportional to C and depends on the dielectric constant of the oxide film ($\epsilon_{Zr} = 23$ for zirconia [31]), on free space permittivity ($\epsilon_0 = 8.85 \times 10^{-14}\ F\,cm^{-1}$) and on the active area of the specimen (surface A_χ in contact with the electrolyte) [29].

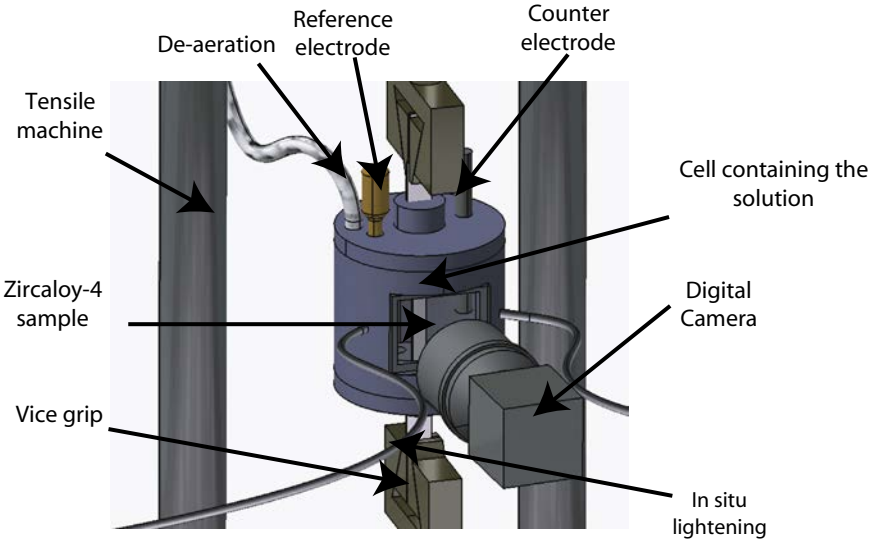

Fig. 4. SCC experimental device.

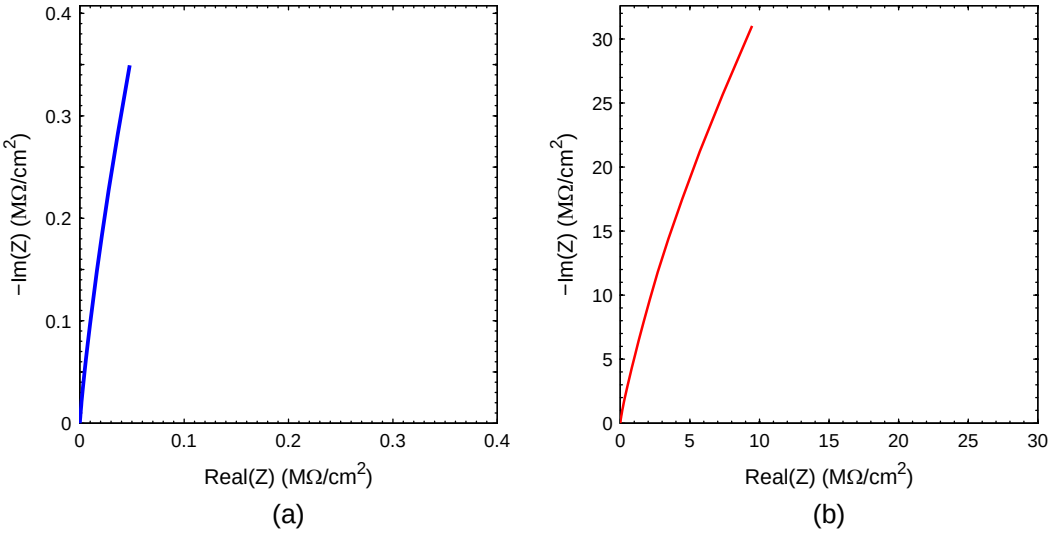

Fig. 5. Nyquist diagram drawn for (a) non-oxidized and (b) oxidized specimens tested by EIS in 0.5 M de-aerated NaCl solution.

This obtained oxide thickness is a little smaller than predicted [20] but remains in the predicted order of magnitude, which is satisfactory considering the asymptotic identification method employed. Accurate C identification actually requires very good surface homogeneity.

Consequently, thermal oxide film is efficient in protecting against pitting corrosion, which localizes only at oxide defects, *i.e.* slip bands emerging at the crack tip. The anodic current density measured during SCC testing is therefore only related to dissolution induced crack propagation.

The effect of the thermal treatment on the pitting potential in both aggressive media was then studied. Cyclic polarization tests were performed on 2.5 × 2.5 cm^2 (exposed area = 4.9 cm^2) Zircaloy-4 coupons at 0.5 mV/s scan rate from Open Circuit Potential (OCP) up to pitting potential (E_{pit}) then reversed. No specific surface preparation was applied to the coupons as oxidation was finally devoted to protecting pre-cracked surfaces from corrosion.

Fig. 6a shows the cyclic polarization curves for two non-oxidized specimens tested in 0.5 M de-aerated NaCl aqueous solutions. Whereas the OCP values differed by 200 mV between the two coupons (which can be due to the heterogeneity of the coupons' surface state), the dissolution current densities appeared to be relatively close together, as well as the obtained pitting potentials: E_{pit}^{nox} (NaCl) ∈ [200–220 mV/SCE]. After reversing the potential, the potential drop associated with repassivation was reproducible and the repassivation potential could be estimated at 80 mV/SCE. After repassivation, current densities were similar. It can therefore be assessed that repassivation is not affected by the initial surface state.

Fig. 6b exhibits the cyclic polarization results obtained for two pre-oxidized coupons in a 0.5 M NaCl solution. Whereas the OCP differed again between the two coupons, passivation currents were reproducible and the corresponding values were lower than the passivation current values of non-oxidized coupons by two orders of magnitude. Protective action of the thermal oxide was therefore confirmed. As expected, the pitting potential E_{pit}^{ox} was higher than previously noted and it may be determined that $\Delta E_{pit} = E_{pit}^{ox} - E_{pit}^{nox}$ = 100 mV. The repassivation potential was the same for both oxidized and non-oxidized coupons. Yet, current values measured after pit repassivation remained much higher than the passivation current values measured before pitting. A re-created passive film was therefore less protective than the initial thermal oxide.

Similar results were obtained in 0.5 M KBr, with a ΔE_{pit} obviously much higher than in the NaCl solution (ΔE_{pit} = 790 mV). Thermal oxidation therefore played a more protective part in pitting in the KBr solution and it can be expected that dissolution current densities during SCC would be much lower in the latter case.

In order to confirm the above results in the situation of SCC, some additional tensile tests were performed under potentiostatic polarization in KBr and NaCl solutions on pre-cracked specimens at different potentials near or below E_{pit}^{nox}. From these tests, it appears that the applied potential must be lower than E_{pit}^{nox} not to obtain a pit on the exposed surfaces but only at the crack tip. This result can be explained by the constant weakening of the oxide induced by strain. The best compromise was obtained for $E_{applied}$ = +150 mV/SCE in a 0.5 M NaCl solution and for $E_{applied}$ = +250 mV/SCE in a 0.5 M KBr solution. These polarization conditions were applied for the following SCC tests monitored by DIC.

4.2. Stress Corrosion Cracking

Pre-cracked and pre-oxidized specimens were submitted to tensile loading (3200 N) while a potential lower than the pitting potential of the non-oxidized metal was applied ($E_{applied}$ = + 150 mV/SCE in a 0.5 M NaCl solution for sample A and $E_{applied}$ = + 250 mV/SCE in a 0.5 M KBr solution for sample B). From the results presented in the previous paragraph, it can be observed that electrochemical activity is concentrated on new non-oxidized surfaces generated during crack propagation.

Fig. 7a shows the evolution of the mode I SIF K_I as a function of time for the tested samples. In Fig. 7b, the evolutions of the crack length with time are depicted. Note that the extension from the initial crack is plotted. The approximate constant crack propagation rate is obtained for both specimens. The average crack rate is 1.05 × 10^8 m/s in NaCl solutions and 0.22 × 10^8 m/s in KBr solutions. This difference in the crack propagation rate can be related to the difference in the SIF evolutions between the two samples. In NaCl, SIF ranging from 25 to 63 MPa$\sqrt{m}$ were obtained. These values were much higher than the one obtained for KBr induced SCC. Indeed, the latter exhibits a SIF value from 20 to 23 MPa$\sqrt{m}$.

SEM observations of fracture surfaces confirm that the use of an aqueous de-aerated NaCl solution as an aggressive medium leads to an enhanced and generalized dissolution process on cracked areas compared to the use of aqueous de-aerated KBr solution. In both cases no pit are observed on gauge length or on the pre-cracked mouth, confirming efficient oxidation protection. Yet, Fig. 8a exhibits large corroded areas on the fracture surface, corresponding to the beginning of the SCC propagation surface. Repassivation is therefore

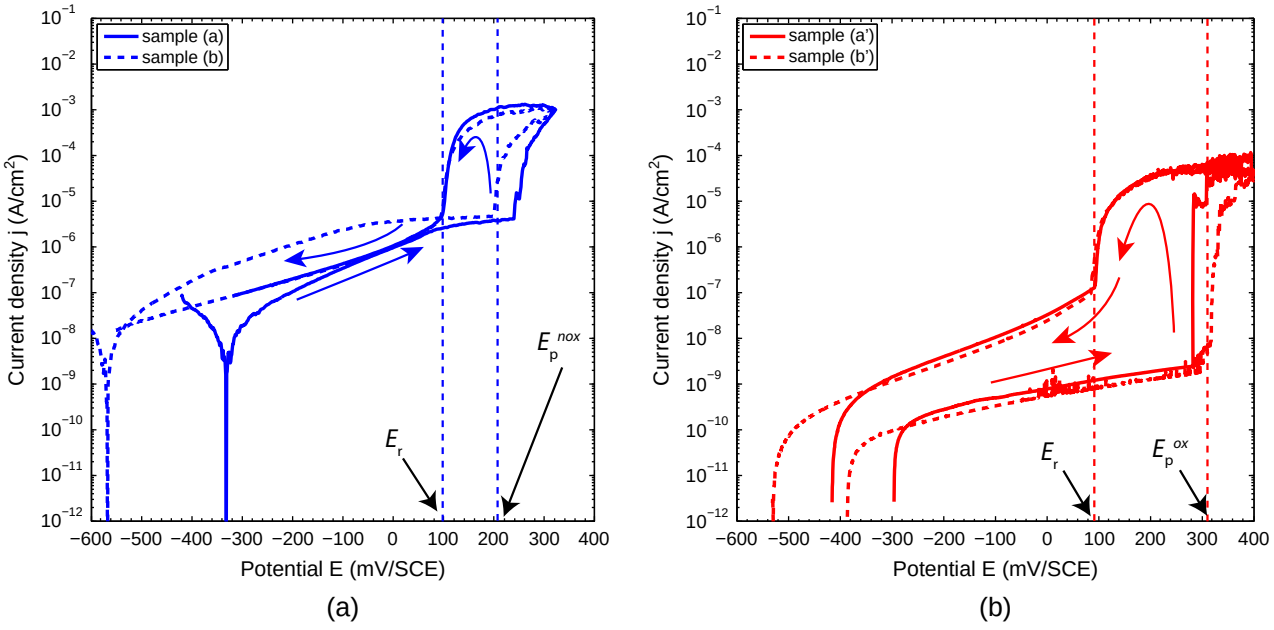

Fig. 6. Cyclic polarization curves for (a) two non-oxidized specimens and (b) two pre-oxidized specimens tested in 0.5 M de-aerated NaCl aqueous solution.

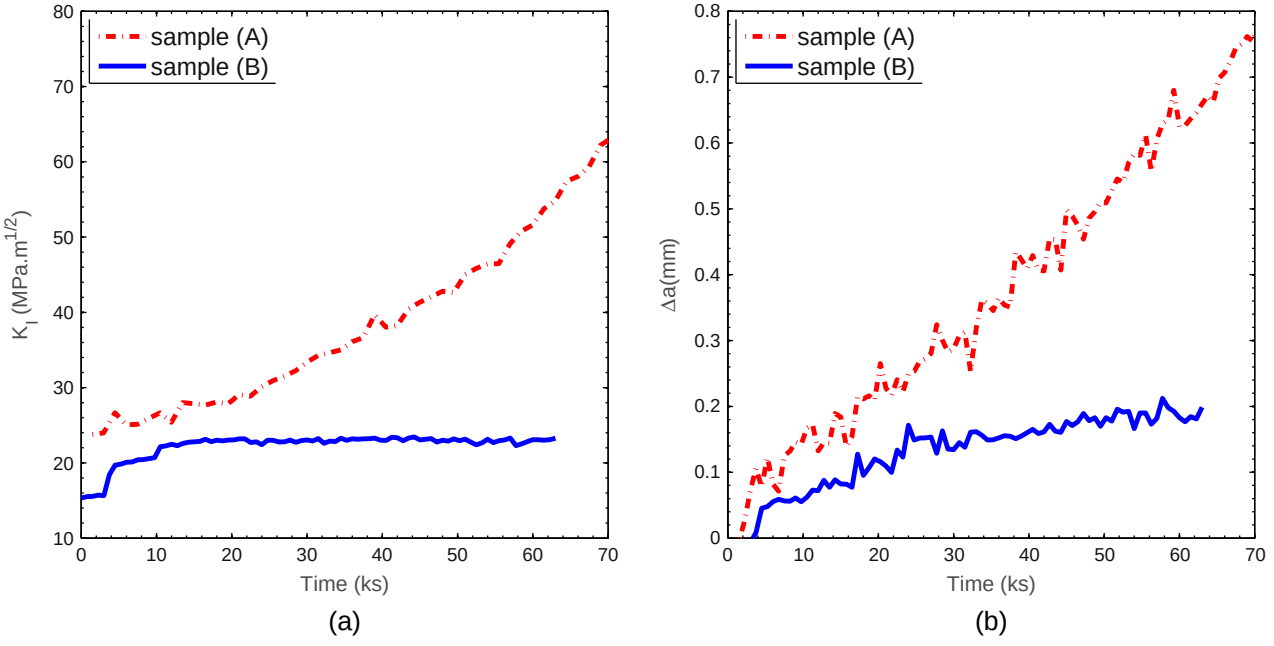

Fig. 7. Evolution of (a) K_I and (b) crack length increment Δa as a function of time during SCC tests (3200 N constant load under potentiostatic polarization: $E_{applied}$ = +150 mV/SCE in a 0.5 M de-aerated NaCl solution for sample A and $E_{applied}$ = +250 mV/SCE in a 0.5 M de-aerated KBr solution for sample B).

limited in the NaCl solution, which prevents us from quantifying active local dissolution at the crack tip. It could be observed some non-corroded small intergranular areas on the fracture surface at the limit of the final ductile failure, which confirmed that the intergranular propagation did not turn into transgranular propagation, as it could be expected for zirconium alloys in halide solutions [13,14,26]. On the other hand, the observation of the fracture surface obtained in KBr solution shows pure intergranular propagation on the entire SCC area with little dissolution traces (Fig. 8b). In this case, the crack mouth repassivates and stress assisted intergranular dissolution is confined to the crack tip. The measured current density is therefore directly representative of localized metal dissolution.

It is finally possible to capitalize the current density values together with the Δa values obtained by DIC and to calculate the height of the active surface h_χ for SCC tests performed in NaCl and KBr solutions according to Eq. (13).

In the NaCl solution, Fig. 9a shows that h_χ increases with the test time to reach 0.1 mm. Indeed, the active surface S_χ does not remain localized at the crack tip but spreads on free surfaces created during crack propagation, as confirmed by SEM observation of the fracture surface (Fig. 8a). In this case, the repassivation of the crack mouth is not ensured due to the presence of depassivating chloride ions. Electrochemical measurements are therefore not representative of dissolution at the crack tip. Consequently, the mechanical solicitation of Zircaloy-4 in a 0.5 M NaCl solution under

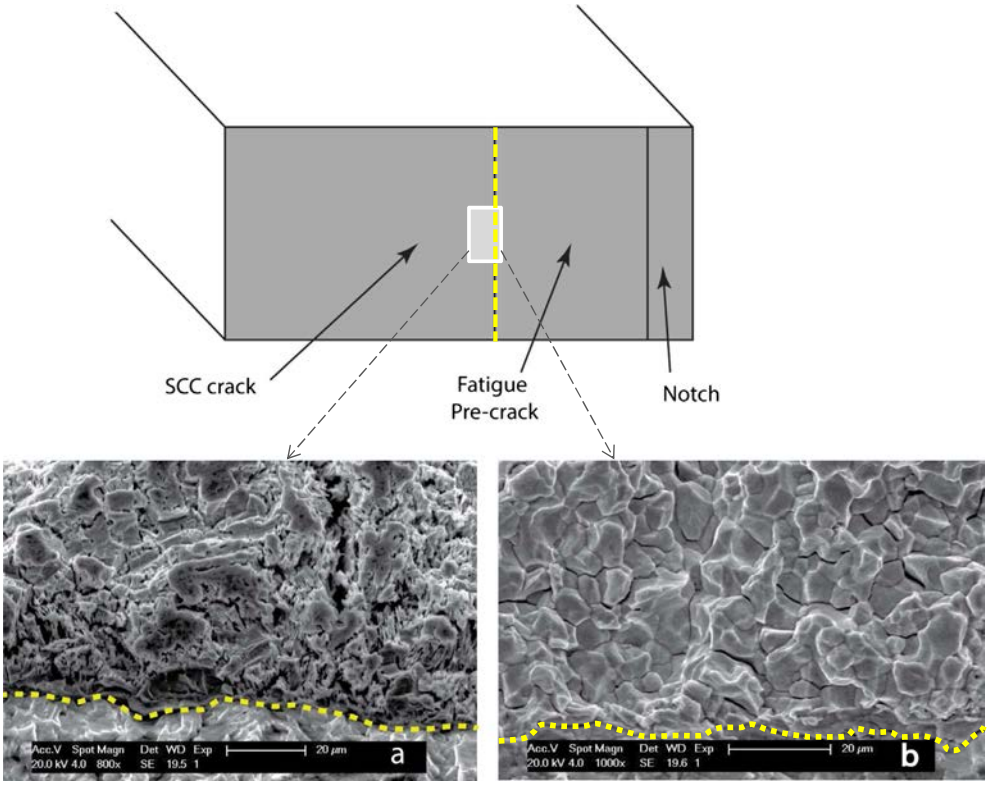

Fig. 8. SEM observation of fracture surfaces of Zircaloy-4 specimens after SSRT conducted in (a) 0.5 M de-aerated NaCl and (b) 0.5 M de-aerated KBr solutions (the dotted line represents the frontier between the fatigue pre-crack and the SCC area).

anodic polarization cannot be described by a true slip dissolution model as failure is not completely brittle. It is confirmed by Green–Lagrange deformations measured on a pre-cracked and oxidized specimen strained by a slow strain rate tensile test in a 0.5 M NaCl solution ($E_{applied}$ = +150 mV/SCE) (Fig. 10b). Strain is located at the crack tip and remains lower than the deformation measured for a specimen strained in air (Fig. 10a). Yet ductility appears to contribute to the rupture of the specimen in this case.

On the other hand, h_χ measured in a KBr solution exhibits a constant and low value (50–80 nm) (Fig. 9b) which is in the order of magnitude of the dissolved grain boundary thickness (Fig. 8b). Green–Lagrange deformation measurements thus confirm the brittle character of the rupture (Fig. 10c). The measured anodic current can be directly related to localized dissolution at the crack tip and it can be assessed that SCC is governed by grain boundary dissolution in the latter case.

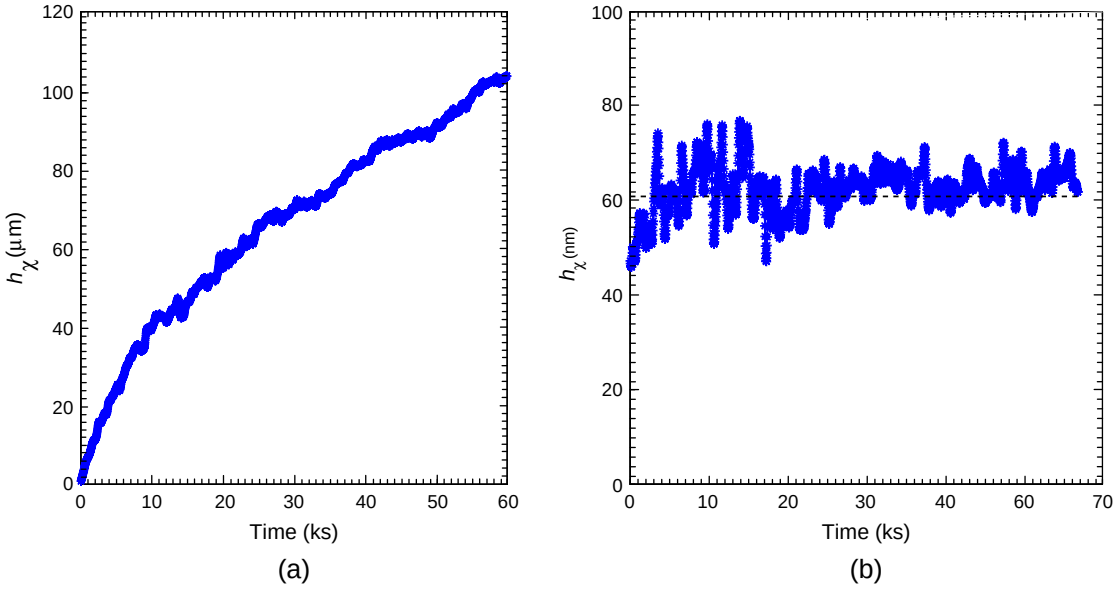

Fig. 9. Height of active surface at the crack tip (from Fig. 1) as a function of time calculated for SCC of Zircaloy-4 in (a) 0.5 M de-aerated NaCl and (b) 0.5 M de-aerated KBr solutions.

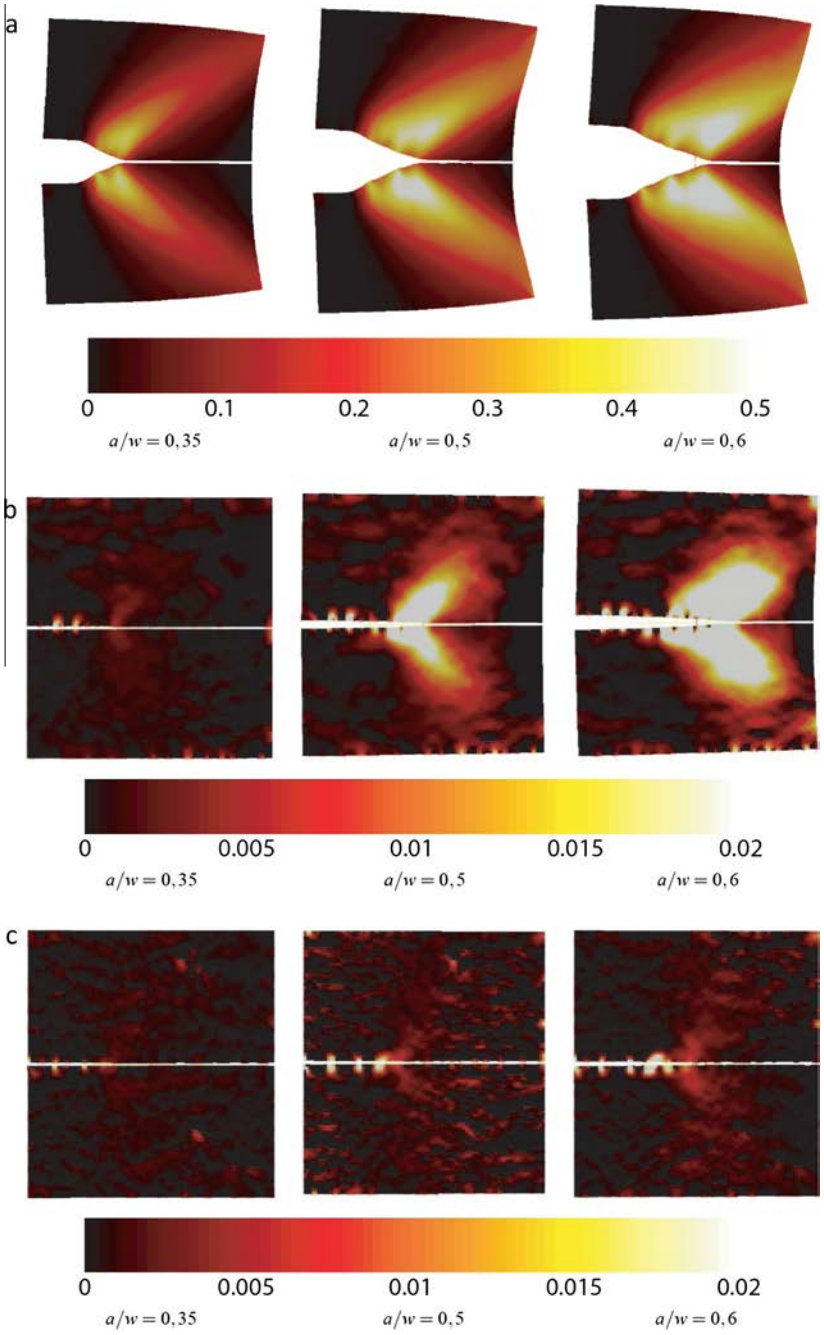

Fig. 10. Green–Lagrange deformations measured on pre-cracked and oxidized specimens strained by slow strain rate tensile test in (a) air, (b) a 0.5 M NaCl solution ($E_{applied}$ = +150 mV/SCE) and (c) a 0.5 M KBr solution ($E_{applied}$ = +250 mV/SCE) (w is the width of the gauge length – see Fig. 3).

5. Conclusion

This study was aimed at (i) proposing a method for localizing electrochemical and mechanical damage processes at the crack tip during SCC propagation and (ii) validating the approach by comparing dissolution current and crack length evolution.

On the one hand, the pre-oxidation of the tensile specimens after pre-cracking and potentiostatic polarization below the pitting potential of non-oxidized Zircaloy-4 allowed us to obtain only a localized dissolution of nude metal provided by slip band emergence at the crack tip. On the other hand, controlled pre-cracking of the notched specimens by load shedding applied to fatigue solicitation allowed us to perform SCC test in well-defined stress state conditions at the crack tip and measure the crack length evolution by DIC.

Two aggressive media were tested. For the NaCl solution the constant repassivation of crack walls was not ensured and rupture exhibits large ductile features. In this case, the direct correlation between the dissolution current and the crack length cannot be obtained. On the other hand, in the case of KBr, fracture remained entirely brittle with the repassivation of crack walls. In the latter case, the correlation between current and crack length measurements provided an estimation of the metal dissolved height at the crack tip which was in accordance with the SEM observation of the resulting intergranular fracture area.

Acknowledgements

The authors are grateful to CEZUS for providing the studied material, and would like to thank Robert di Folco from the MATEIS Lab for his technical support.

References

[1] H. Czichos, T. Saito, L. Smith, Handbook of Materials Measurement Methods, Springer, Berlin, 2006, pp. 611–684.
[2] F. Ford, Slip dissolution model, in: Corrosion sous contrainte, phénoménologie et mécanismes, EDP Science, 1990, pp. 307–344.
[3] J. Galvele, J. Nucl. Mater. 229 (1996) 139–148.
[4] Z. Lu, T. Shoji, J. Pressure Vessel Technol. 128 (3) (2006) 318–327.
[5] M. Hall, Corros. Sci. 50 (10) (2008) 2902–2905.
[6] T. Anita, M.G. Pujar, H. Shaikh, R.K. Dayal, H.S. Khatak, Corros. Sci. 48 (2006) 2689–2710.
[7] G. Du, J. Li, W.K. Wang, C. Jiang, S.Z. Song, Corros. Sci. 53 (9) (2011) 2918–2926.
[8] M. Breimesser, S. Ritter, H.P. Seifert, T. Suter, S. Virtanen, Corros. Sci. 63 (2012) 129–139.
[9] D.B. Wells, J. Stewart, R. Davidson, P.M. Scott, D.E. Williams, Corros. Sci. 33 (1) (1992) 39–71.
[10] M. Leban, Ž. Bajt, A. Legat, Electrochim. Acta 49 (2004) 2795–2801.
[11] J. Kovac, M. Leban, A. Legat, Electrochim. Acta 52 (2007) 7607–7616.
[12] B. Cox, J. Nucl. Mater. 170 (1) (1990) 1–23.
[13] S. Farina, G. Duffo, J. Galvele, Corros. Sci. 45 (11) (2003) 2497–2512.
[14] S. Farina, G. Duffo, Corros. Sci. 46 (9) (2004) 2255–2264.
[15] T. Shoji, Z. Lu, H. Murakami, Corros. Sci. 52 (3) (2010) 769–779.
[16] T. Tay, C. Yap, C. Tay, Eng. Fract. Mech. 52 (5) (1995) 879–885.
[17] J. Kovac, C. Alaux, T.J. Marrow, E. Govekar, A. Legat, Corros. Sci. 52 (6) (2010) 2015–2025.
[18] A. Stratulat, J.A. Duff, T.J. Marrow, Corros. Sci. 85 (2014) 428–435.
[19] S. Ritter, D.A. Horner, R.-W. Bosch, Corros. Eng., Sci. Technol. 47 (4) (2012) 251–264.
[20] J.A. Duff, T.J. Marrow, Corros. Sci. 68 (2013) 34–43.
[21] M. Williams, ASME J. Appl. Mech. 24 (1957) 109–114.
[22] S. Roux, F. Hild, Int. J. Fract. 140 (1) (2006) 141–157.
[23] E. Durif, J. Rethore, A. Combescure, M. Fregonese, P. Chaudet, Exp. Mech. 52 (2012) 1021–1031.
[24] Q. Peng, J. Kwon, T. Shoji, J. Nucl. Mater. 324 (1) (2004) 52–61.
[25] L. Gosmain, C. Valot, D. Ciosmak, O. Sicardy, Solid State Ionics 141 (2001) 633–640.
[26] P. Sidky, J. Nucl. Mater. 256 (1) (1998) 1–17.
[27] J. Jorcin, PhD thesis, Institut National Polytechnique de Toulouse, France, 2007.
[28] O. Lavigne, C. Alemany-Dumont, B. Normand, M.H. Berger, C. Duhamel, P. Delichère, Corros. Sci. 53 (6) (2011) 2087–2096.
[29] A. Satpati, S. Phadnis, R. Sundaresan, Corros. Sci. 47 (6) (2005) 1445–1458.
[30] B. Normand, H. Takenouti, M. Keddam, H. Liao, G. Monteil, C. Coddet, Electrochim. Acta 49 (17-18) (2004) 2981–2986.
[31] D. Thompson, A. Dickins, J. Thorp, J. Mater. Sci. 27 (8) (1992) 2267–2271.